

Echoes of a decaying planetary system: the gaseous and dusty disks surrounding three white dwarfs

C. Melis^{1,2}, M. Jura¹, L. Albert³, B. Klein¹, B. Zuckerman¹

cmelis@ucsd.edu

ABSTRACT

We have performed a comprehensive ground-based observational program aimed at characterizing the circumstellar material orbiting three single white dwarf stars previously known to possess gaseous disks. Near-infrared imaging unambiguously detects excess infrared emission towards Ton 345 and allows us to refine models for the circumstellar dust around all three white dwarf stars. We find that each white dwarf hosts gaseous and dusty disks that are roughly spatially coincident, a result that is consistent with a scenario in which dusty and gaseous material has its origin in remnant parent bodies of the white dwarfs' planetary systems. We briefly describe a new model for the gas disk heating mechanism in which the gaseous material behaves like a “Z II” region. In this Z II region, gas primarily composed of metals is photoionized by ultraviolet light and cools through optically thick allowed Ca II-line emission.

Subject headings: circumstellar matter — planet-star interactions — stars: individual (Ton 345, SDSS J122859.93+104032.9, SDSSJ104341.53+085558.2) — white dwarfs

1. Introduction

White dwarfs represent the endstate of stellar evolution for the majority of stars within our galaxy. Most stars with mass less than $\sim 8 M_{\odot}$ will end up as these exposed cores of nuclear ash that slowly cool over time as they radiate away their energy. The planetary

¹Department of Physics and Astronomy, University of California, Los Angeles, CA 90095-1547, USA

²Current address: Center for Astrophysics and Space Sciences, University of California, San Diego, CA 92093-0424, USA

³CFHT Resident Astronomer, 65-1238 Mamalahoa Highway, Kamuela, HI 96743, USA

systems that may have orbited these white dwarfs while they were on the main sequence have been shown to be able to survive through the asymptotic giant branch (AGB) phase of stellar evolution (Sackmann *et al.* 1993; Duncan & Lissauer 1998; Debes & Sigurdsson 2002; Burleigh *et al.* 2002). What is the ultimate fate of these remnant planetary systems?

The work of Duncan & Lissauer (1998) showed numerically that giant planets orbiting white dwarfs descendent from massive progenitor stars are likely to become dynamically unstable on timescales less than ~ 10 Gyr. Less massive progenitor stars are more likely to have giant planets with stable orbits at the end of their stellar evolution. However, these less massive progenitor stars are also expected to obliterate any terrestrial-like planets orbiting within ~ 1 AU during their AGB evolutionary phase, whereas all terrestrial planets around more massive stars will likely survive through the AGB (e.g., Sackmann *et al.* 1993). Rocky objects; like comets, asteroids, or terrestrial planets; are expected to survive to the white dwarf evolutionary phase for a variety of initial sizes and orbital semi-major axes (Jura 2008), but may suffer orbital de-stabilization through the perturbations of giant planets and be flung towards the white dwarf star (Debes & Sigurdsson 2002).

Once within the white dwarf’s Roche radius, rocky bodies will be tidally shredded and eventually accrete onto the white dwarf’s photosphere (Debes & Sigurdsson 2002; Jura 2003a; Zuckerman *et al.* 2007; Klein *et al.* 2010; Dufour *et al.* 2010). Sub-micron size grains orbiting within the Roche radius of their host white dwarf star can produce a noticeable infrared excess above what would be expected from the white dwarf photospheric emission alone. Directly detecting rocky objects in orbit around white dwarfs will be exceedingly difficult; in contrast, the dusty finale of rocky objects that fall into a white dwarf’s Roche radius and the eventual atmospheric pollution from the residual rocky object material leave a tell-tale sign that there is a dissolving remnant planetary system. Thus, much like current searches around main sequence stars utilize debris disks as signposts for planetary systems (e.g., Zuckerman & Song 2004; Krivov 2010), remnant rocky planets around white dwarfs are currently best investigated indirectly through searches for white dwarf debris disks and atmospheric pollution.

Past searches for remnant planetary systems around white dwarfs have focused on direct and indirect detection of giant planet companions (e.g., Hogan *et al.* 2009; Mullally *et al.* 2008, and references therein) and the detection of dust contained within a white dwarf’s Roche radius as discussed above (e.g., Farihi *et al.* 2009, and references therein). To date, searches for giant planets have had little success (but see Mullally *et al.* 2008, 2009). The first evidence for a remnant planetary system around a white dwarf came from the work of Zuckerman & Becklin (1987) in which it was discovered that the nearby white dwarf star G29–38 hosted infrared excess. This infrared excess was interpreted by Zuckerman & Becklin

(1987) to probably be the signature of a brown dwarf companion. However, subsequent observations of G29–38 found evidence for a silicate emission feature at $\sim 10\ \mu\text{m}$ (Graham *et al.* 1990; Tokunaga *et al.* 1990; Reach *et al.* 2005) indicating that the excess originated from a dusty debris disk. Further ground-based investigation of white dwarfs decades later revealed three new debris disks (Becklin *et al.* 2005; Kilic *et al.* 2005, 2006; Kilic & Redfield 2007). It took the launching of the mid-infrared optimized Spitzer Space Telescope (Werner *et al.* 2004) to obtain the necessary sensitivities to probe for a statistical sample of debris disk-hosting white dwarfs. Spitzer proved excellent at discovering debris disks around white dwarf stars, increasing the sample size by nine (see Table 1 in Farihi *et al.* 2009, and references therein). Spitzer observations that reached white dwarf photospheric flux levels enabled a statistical measure of the incidence of white dwarf debris disks. Farihi *et al.* (2009) compiled all previous Spitzer observations and found that $\sim 1\text{--}3\%$ of all single white dwarfs with cooling ages $\lesssim 0.5\ \text{Gyr}$ ($T_{\text{eff}} \sim 10,000\text{--}20,000\ \text{K}$) have debris disks and that $\sim 50\%$ of white dwarfs with implied metal accretion rates of $\dot{M} > 3 \times 10^8\ \text{g s}^{-1}$ have dusty material orbiting them. All white dwarfs discussed above have debris disks contained almost entirely within their respective white dwarf’s Roche radius indicating disrupted rocky objects.

Contemporaneous with the Spitzer white dwarf disk searches, Gänsicke *et al.* (2006) noted peculiar double-peaked gas emission lines from a hot ($T_{\text{eff}} = 22,000\ \text{K}$) white dwarf observed as part of the Sloan Digital Sky Survey (SDSS; York *et al.* 2000). This single white dwarf, dubbed SDSS 1228+1040 (spectral type DAZ), was interpreted to have an orbiting gaseous metal disk that had its origin in disrupted asteroidal material. Searches through the rest of the SDSS white dwarf spectroscopic database uncovered two more gas-disk white dwarfs (SDSS1043+0855, DAZ, and SDSS0843+2257, DBZ; Gänsicke *et al.* 2007, 2008a, hereafter SDSS1043 and Ton 345). Spitzer and ground-based observations of SDSS 1228+1040¹ (hereafter SDSS1228) show that this gas disk-hosting white dwarf is also orbited by dusty material that coincides positionally with the gaseous material (Brinkworth *et al.* 2009). Such a discovery heralds the use of such gas and dust disk hosting white dwarfs as benchmark objects for studying the decay of planetary systems as the two disk components yield complementary insights; for example, gas disk measurements can directly inform one about the dynamics of the disk while dust disk modeling indirectly provides information about disk structure.

Through judicious observing with both ground- and space-based facilities there is now convincing evidence that white dwarfs show signs of dissolving planetary systems. However,

¹Farihi *et al.* (2010) performed AKARI observations of Ton 345 that indicate there is excess infrared emission at 2.3, 3.2, and 4.3 μm ; these observations are contaminated by a nearby background object discussed in Section 2.

the sample size of debris disk white dwarfs is still small and would benefit from additional objects. Furthermore, it is not yet clear how the gas disk white dwarfs fit into the dissolving planetary system framework that explains the white dwarf debris disk observations. Thus, in an effort to better understand the final throes of planetary system evolution, ground-based near-infrared and optical spectroscopic observations of the three gas-disk systems discovered by Gänsicke *et al.* (2006, 2007, 2008a) were performed and are reported herein.

2. Observations

2.1. WIRCam Imaging at the CFHT

Initial near-infrared (NIR) images of Ton 345 and SDSS1043 were obtained with WIRCam mounted on the 3.6-m CFHT telescope (Puget *et al.* 2004) on the nights of UT 24 February 2008 and UT 19 June 2008, respectively. We used a 6- to 9-point dither pattern with 60'' offsets between dithers. For Ton 345 we took exposures in the J, H, and K_s bands with 45, 15, and 25 seconds per dither (yielding total integration times of 270, 630, and 450 seconds, respectively). The H-band observations for Ton 345 were repeated on UT 25 February 2008 in better sky brightness conditions. Both H-band data sets yielded the same result. For SDSS1043 we took exposures only in the K_s-band; these observations were performed in a manner similar to that described for Ton 345. Images were preprocessed, non-linearity corrected, and sky subtracted at CFHT with the ‘Iwi pipeline² and median-stacked using the suite of Terapix software (`sExtractor` - Bertin & Arnouts (1996), `scamp` - Bertin (2006), and `swarp`³) with the 2MASS point-source catalogue as the reference for external astrometry. Photometry of the two white dwarfs and all 2MASS sources was performed using the FLUX_AUTO measurement in SExtractor, version 2.4.4. Absolute photometry was anchored on the 2MASS system using a weighted average of all (>200) 2MASS point sources in the full field of view and 5 iterations of 3 σ outlier rejection. The uncertainty on this calibration is ~ 0.03 magnitudes in all three bands for objects with fluxes similar to Ton 345 and ~ 0.05 magnitudes in K_s for objects similar in flux to SDSS1043.

WIRCam data for Ton 345 are summarized in Table 1 which also includes SDSS and GALEX fluxes. Images of Ton 345 and a $\sim 1.8''$ separation background source, presumably a galaxy, are displayed in Figure 1. Large beam instruments (like Spitzer or AKARI) would be contaminated by this red background object. The WIRCam result for SDSS1043 is presented

²<http://www.cfht.hawaii.edu/Instruments/Imaging/WIRCam/IwiVersion1Doc.html>

³<http://www.astromatic.net/>

in Table 2.

2.2. NIRI Imaging at Gemini-North

Follow-up observations of Ton 345 were obtained with NIRI (Hodapp *et al.* 2003) mounted on the Gemini North Telescope. Observations were performed on UT 24 May 2008 during Director’s Discretionary Time (program GN-2008A-DD-5). 5-point dither pattern image sets were repeated for J, H, and K_s with total integration times of 105, 120, and 150 seconds, respectively. A 4-point dither pattern was repeated for L’ until we accrued a total integration time of 2520 seconds.

After pre-processing to correct for the known NIRI non-linearity⁴, data were reduced using in-house IDL software routines. For each filter, science frames were median combined to generate a “sky-median” frame which was then subtracted from each science frame. Sky-subtracted frames were then flat-fielded using exposures of the illuminated telescope dome for J, H, and K_s. L’ frames were flat-fielded using the median stack of all science frames normalized to unity. Reduced science frames were registered by reversing the header-recorded values for the telescope offsets between dithers.

Photometric measurements for Ton 345 were calibrated by comparing extracted fluxes for each filter to standard stars fluxes (Leggett et al 2003, 2006) observed and reduced in a similar fashion. For JHK_s the standard star was FS 15, for L’ it was HD 84800. We note that HD 84800 appears to have a $\sim 0.4''$ extent in our L’ images; no telescope problems were noted at the time of observation. JHK_s fluxes were extracted with an aperture that yielded $\sim 85\%$ encircled energy (with a negligible difference between Ton 345 and FS 15). For L’ flux calibration we used a $2.0''$ diameter aperture to extract the flux of HD 84800 and Ton 345. Uncertainties for JHK_s fluxes were determined by examining the dispersion of the extracted fluxes for each of the individual reduced science frames. Since this was not possible in our L’ imaging sets, we instead made ten randomly placed extractions on the final, median-stacked L’ image using the same aperture that was used to extract the flux for Ton 345. The standard deviation of this set of values was adopted as the flux measurement uncertainty. The final signal-to-noise ratio (S/N) is ~ 50 for JHK_s while for L’ it is $\sim 3-5$.

NIRI photometric results are listed in Table 1. Figures 1 and 2 show the NIRI images of Ton 345 and the $\sim 1.8''$ separated galaxy. Table 3 lists fluxes for the galaxy extracted using similar apertures and procedures as for Ton 345.

⁴<http://staff.gemini.edu/~astephens/niri/nirlin/>

2.3. Gemini Imaging at the Shane 3-m

Observations of SDSS1043 in the J-band were performed UT 10 October 2008 with the Gemini Twin-Arrays Infrared Camera (McLean *et al.* 1993) mounted on the 3-m Shane telescope at Lick Observatory. We used a 5 position dither pattern with 20 second integrations of 5 coadds per position resulting in 500 seconds total on source integration time. The $\sim 3'$ field-of-view of the Gemini instrument enabled simultaneous observations of two 2MASS stars for use in flux calibration. Although Gemini hosts two infrared cameras, data for the longer wavelength chip were unusable due to instrumental difficulties.

Data were reduced and fluxes extracted much like that described above for the Ton 345 NIRI data. Exceptions include no non-linearity correction, the use of twilight flats instead of dome flats, and image registration using bright point sources within the field. The Gemini J-band flux for SDSS1043 is reported in Table 2.

2.4. HIRES Spectroscopy

Keck HIRES (Vogt *et al.* 1994) optical echelle spectra were obtained for each of the gas-disk white dwarfs. Table 4 lists observation dates and HIRES instrumental setups. Data were reduced via two software packages: IRAF and MAKEE. Standard IRAF tasks were used in the reduction and extraction of the HIRES data. After reduction and extraction, low order polynomials were fit to each order to bring overlapping order segments into agreement.

The output of each software package was compared to ensure no reduction artifacts were contaminating gaseous emission lines. We found that additional processing steps were necessary for data taken in the red setup. In some observing setups blue light in second order leaked into the ~ 8200 to 9000 \AA range. This could potentially “veil” absorption and emission lines in this region, especially the Ca II $\lambda 8662$ transition. To estimate the contaminating flux present we extrapolated the flux from blue contaminant orders that fell in between red orders. We believe that this excess flux was removed for most observations, only the 2008 November observations of SDSS1228 and SDSS1043 might have significant residuals due to strong Balmer absorption lines that were difficult to model.

3. Results

3.1. Imaging

Table 1 lists measured near-infrared fluxes for Ton 345 from the CFHT and Gemini North data sets. To place these near-infrared measurements in context we queried SDSS DR7 (Abazajian *et al.* 2009) and GALEX for *ugriz* and ultraviolet fluxes, respectively. From the measured magnitudes alone it is apparent that Ton 345 hosts significant near-infrared excess (see Section 4).

Table 2 lists GALEX ultraviolet fluxes, SDSS *ugriz*, and the ground-based near-infrared photometry for SDSS1043. Our data alone do not conclusively show that there is infrared excess emission towards SDSS1043. But, when these ground-based near-infrared measurements are combined with Spitzer photometry at longer wavelengths (C. Brinkworth *et al.* 2010, in preparation), significant excess infrared emission is apparent (see Section 4).

3.2. Optical Spectroscopy

Double-peaked metallic gas emission lines are detected towards all three white dwarfs. Emission lines from Ca II and Fe II are shown in Figures 3 and 4. Ca II H & K emission lines are detected only for SDSS1228 (Figure 3 and Table 5). Fe II $\lambda 5169$ emission lines are detected for SDSS1228 and Ton 345 (Figure 3, Figure 4, and Table 5). Fe II $\lambda 5018$ emission lines for SDSS1228 that were noted by Gänsicke *et al.* (2006) are not detected. Measurable quantities from emission features in the spectra, and associated derived quantities, can be found in Tables 5 and 6. We defer quantitative analysis of absorption feature equivalent widths and elemental abundances to future publications.

Table 5 contains information on the velocity separation between emission peaks of the same transition, the full velocity width at zero power of each double-peaked emission feature, the “peak midpoint”, and the maximum velocity gas detected in the blue and red wings of the double-peaked emission features ($v_{\max} \sin i$). We estimate the wavelength centroid position of emission peaks by fitting either Gaussian or Lorentzian profiles over a $\sim 10\text{--}15$ Å range centered on the emission line peak. Three to four fits per peak are performed with the continuum anchor points for the fitting function at different locations within the noise of the spectrum. The peak centroid is taken to be the average of these multiple fits while an estimate of the uncertainty on the centroid comes from the standard deviation of these fits. The peak midpoint position is then determined by averaging the two emission peak centroids for each transition. The peak centroid and peak midpoint wavelength values are converted

into velocities relative to the rest wavelength for the corresponding transition they are being measured from.

Measured radial velocities for each star are reported in the second column of Table 6. We compute Galactic UVW space motions using the gravitational redshift-corrected radial velocities (where gravitational redshifts in Table 6 are computed using the stellar parameters of Gänsicke *et al.* 2006, 2007, 2008a, which are reproduced in Table 6), 2MASS sky positions (Cutri *et al.* 2003), proper motion information from the NOMAD catalog (Zacharias *et al.* 2004), and distances computed from the $R_{WD}/Dist$ parameter from our model fits (see Section 4 and Table 7) and the gravity values given in Gänsicke *et al.* (2006, 2007, 2008a). We adopt an uncertainty of 10% for the distances.

3.2.1. Gas Disk Evolution

With multiple epochs of spectra, and by comparison to the Ca II IRT emission lines presented in Gänsicke *et al.* (2006, 2007, 2008a), we can probe variability in emission line strength and morphology. Table 5 contains emission line equivalent widths, velocity separation between emission peaks of a given transition, and the full width at zero power of emission lines for each epoch a gas emission line was observed. Figure 4 shows multiple epochs of Fe II $\lambda 5169$ emission lines for SDSS1228 and Ton 345 and multiple epochs of Ca II IRT emission in Ton 345. There are no significant variations detected in the Fe II emission lines (but see caption to Figure 4).

Ton 345’s Ca II IRT emission line equivalent widths and morphologies appear to agree to within the errors associated with each individual HIRES epoch. This is in contrast to the two epochs presented in Gänsicke *et al.* (2008a) in which the equivalent width of the sum of the three Ca II IRT lines decreases by a factor of ~ 1.5 and a significant morphological change in the emission profile is seen between 2004 Dec and 2008 Jan. The measurements for the sum of the Ca II IRT emission equivalent width reported herein agree with the Gänsicke *et al.* (2008a) 2008 Jan value to within the 1σ errors. Although speculative, this might suggest that an episodic disk feeding event occurred before the 2004 Dec epoch and that the 2008 measurements are probing a “quiescent” phase.

Comparing the HIRES observations of SDSS1228’s Ca II IRT complex to those presented in Gänsicke *et al.* (2006, 2007) suggests the stronger of the two emission peaks has switched from the red side of the double peaked emission complex (as seen in Gänsicke *et al.* 2006, 2007) to the blue side (HIRES data). This parity switch in the peak strength is confirmed when we degrade the HIRES data to the resolution of the spectra presented in Gänsicke *et al.*

(2006). Interpretation of this parity switch is complicated by the sparse time sampling of the emission line complexes. The Gänsicke *et al.* (2006, 2007) spectra have epochs of 2003 Mar (SDSS) and 2006 Jul (WHT). The morphological appearance of the Ca II IRT emission lines in the SDSS and WHT spectra suggests little change between these two epochs. It is not clear what would change the parity in the emission peak strength between the 2006 WHT epoch and the 2008 HIRES epoch. One possibility is that the disk is clumpy and we have witnessed the clumps orbiting around SDSS1228. Additional spectroscopic monitoring of SDSS1228 is necessary to confirm and characterize such orbiting clumps.

4. Dust Disk Parameters

Ton 345’s photometry suggests near-infrared emission in excess of what one would expect from the photosphere of the white dwarf star alone. The comprehensive data set in Table 1 is modeled as a flat, passive, opaque disk (Jura 2003b; Jura *et al.* 2007a) orbiting a $\sim 18,600$ K effective temperature white dwarf. Ton 345’s photospheric emission is assumed to be well represented by a blackbody curve; such a model is reasonable for Helium dominated atmosphere white dwarfs that do not exhibit strong ultraviolet flux suppression from Hydrogen absorption. Figure 5 displays the white dwarf and disk model while Table 7 reports the model parameters. The photospheric and excess fluxes are reproduced successfully by the white dwarf and disk model. However, because the measurements used for Ton 345 only extend out to wavelengths as long as L' , the temperature at the outer edge of the dust disk is observationally unconstrained. In the model shown in Figure 5 and Table 7 we assume T_{outer} of the disk is 1000 K. T_{outer} could be, and likely is, smaller than this value (see below). Further observational constraint of the disk outer edge temperature will require longer wavelength data that is uncontaminated by the nearby background object.

In the interest of comparing a homogeneous set of disk model parameters, we refit the data for SDSS1228 presented in Brinkworth *et al.* (2009) and the data for SDSS1043 presented in C. Brinkworth *et al.* (2010, in preparation) in the same manner as Ton 345. These model fits and measured fluxes are shown in Figures 6 and 7 with model parameters reported in Table 7. It is noted that SDSS1043’s outer disk temperature is poorly constrained even with the inclusion of IRAC photometry. In an effort to illustrate the range of viable model parameters that can fit the measured infrared excesses, we plot in Figure 6 three models for SDSS1228 that have different dust disk parameters (Table 7). The resultant parameter extremes reported in Table 7 are taken to be the $\sim 5\sigma$ confidence limit on each model parameter. We then derive the 1σ model parameter uncertainties by dividing the difference between parameter extremes by five; these uncertainties are reported along with

SDSS1228’s best fit model parameters in Table 7.

For the case of optically thick, flat dust disks Eq. 1 from Jura (2003b) can be used to determine at what radial distance from each white dwarf dust particles of certain temperatures reside. As previously mentioned, for Ton 345 and SDSS1043 the temperature of the outer region of their orbiting dusty material is poorly constrained by observations. Rather than take the model outer disk temperatures for Ton 345 and SDSS1043 (which are better interpreted as upper limits), we instead estimate their outer disk temperatures under the assumption of an asteroidal debris model for the origin of the dusty disk. Such a scenario requires a rocky object to fall within the Roche radius of the white dwarf (Debes & Sigurdsson 2002; Jura 2003b). The following expression for the Roche radius is used (Davidsson 1999):

$$R_{tide} = C_{tide} \left(\frac{\rho_*}{\rho_a} \right)^{1/3} R_*$$

where within R_{tide} (the radial separation from a star of radius R_* and density ρ_*) a rocky object of density ρ_a would be disrupted. The factor C_{tide} is a constant of order unity that is determined by the tensile strength, shape, rotation rate, and orbital parameters of the rocky object (Davidsson 1999; Holsapple & Michel 2008). It is unlikely that all objects that were tidally shredded around SDSS1228, Ton 345, and SDSS1043 had the same physical parameters; however, in the absence of any such information it is assumed that this is the case. Such an assumption can potentially introduce a significant systematic offset in the derived outer dust disk radii. Using the well-modelled data for SDSS1228 (Table 7) and assuming an asteroid density of $\sim 3 \text{ g cm}^{-3}$ a value of 1.45 for C_{tide} is estimated. Combining these values with the mass and radius of the white dwarfs (see Table 6) from Gänsicke *et al.* (2006, 2007, 2008a) we calculate the tidal radii for each white dwarf. These values for Ton 345 and SDSS1043 are reported as $R_{outer,dust}$ in Table 8. The value reported for SDSS1228 in Table 8 is the disk outer radius as derived from fitting its Spitzer data.

5. Gas Disk Parameters

Using the HIRES optical spectra we can estimate the radial extent of the gaseous disks orbiting the three white dwarfs. This is done by measuring the highest velocity gas emission in the HIRES spectra ($v_{\max} \sin i$ in Table 5), emission that corresponds to the innermost orbit of the emitting gas-phase metals around the white dwarf (e.g., Horne & Marsh 1986). However, this value is degenerate with the inclination angle of the disk, i , where the degeneracy is $v \sin i$ (i of 0° would correspond to a face-on disk). The dust disk model fits (Section 4) can help constrain the disk inclination angle assuming the dust and gas disks are coplanar. It is

noted that the inclination angles as derived from the dust disk fitting can vary by $\sim 20\text{--}30\%$ from the best-fit value (5σ ; see Table 7 and Section 4). Line-of-sight gas disk velocities for the three white dwarfs are corrected using the dust disk model best-fit inclination angles. Assuming Keplerian orbits of the gas and dust disks, we use the white dwarf masses and radii (see Table 6) as modeled by Gänsicke *et al.* (2006, 2007, 2008a) to derive the gas disk inner radius in units of white dwarf radii. We obtain the full dimensions of the gaseous disks by combining these measurements with the Gänsicke *et al.* (2006, 2007, 2008a,b) models (see Section 6) in which the gas disk outer radii have been estimated. These results are reported in Table 8 and illustrated in Figure 8.

We note the discrepancy between our inferred gas disk inner radius for SDSS1228 and the same as quoted in Brinkworth *et al.* (2009). The origin of this discrepancy has to do with two factors. The first factor is responsible for the smaller gas disk inner radius quoted in Brinkworth *et al.* (2009) – $R_{\text{inner,gas}} \sim 27 R_{\text{WD}}$ – and results from use of the maximum Ca II infrared triplet (IRT) gas emission velocity of $\sim 1270 \text{ km s}^{-1}$ as reported in Table 1 in Gänsicke *et al.* (2006). Re-measurement of the spectra presented in Gänsicke *et al.* (2006) provides a maximum gas emission velocity more in line with that measured herein (Table 5; use of the Gänsicke *et al.* 2006, erroneous $v_{\text{max}} \sin i$ will reduce the gas disk inner radius by a factor of ~ 1.8 relative to our inferred gas disk inner radius) and what is quoted in the supplementary material of Gänsicke *et al.* (2006)⁵. The second factor is a 20% increase in the inner disk radius relative to that presented herein (where the ratio of $1.8/1.2=1.5$ is the ratio between our inferred gas disk inner radius and that of Brinkworth *et al.* 2009) and comes from a matter of interpreting Figure 1 of Horne & Marsh (1986). The inner gas disk radius reported in Table 8 for SDSS1228 agrees with the value quoted in the supplementary material to Gänsicke *et al.* (2006)⁵.

5.1. Stable Eccentric Disk at Ton 345

Here a novel method of estimating the gravitational redshift for the gas disk-hosting white dwarf stars is attempted. This method employs the gas disk emission lines (from which we seek to measure the white dwarf systemic velocity) and photospheric absorption lines (which contain velocity components from the systemic velocity and the gravitational redshift from the compact white dwarf). To estimate the gravitational redshift we measured the photospheric absorption line radial velocity for each white dwarf (see RV_{obs} in Table

⁵The values reported in the main article text and tables of Gänsicke *et al.* (2006) are different from those reported in the supplementary online material.

6) and the systemic radial velocity for each white dwarf-disk system from gaseous emission lines (see “Peak Midpoint Velocity” in Table 5 and discussion in Section 3.2). Our estimated gravitational redshift for SDSS1228 ($RV_{\text{obs}} - [\text{Peak Midpoint Velocity}]_{\text{avg}} = 55 \pm 5 \text{ km s}^{-1}$; based only on the Ca II IRT emission lines) reproduces well the expected gravitational redshift (44 km s^{-1} , see Table 6). Estimates for SDSS1043 are inconclusive due to the low S/N in the gas emission lines. However, our estimate for Ton 345 ($RV_{\text{obs}} - [\text{Peak Midpoint Velocity}]_{\text{avg}} = 131 \pm 6 \text{ km s}^{-1}$; based only on the Ca II IRT emission lines) is quite different from the expected gravitational redshift (44 km s^{-1}).

Why does this method fail for Ton 345? A clue comes from considering the agreement of SDSS1228’s gravitational redshifts as measured from the two different methods. As modeled by Gänsicke *et al.* (2006, 2008a), the gas disk orbiting SDSS1228 has negligible eccentricity while for Ton 345 the disk eccentricity is large ($e \sim 0.2 - 0.4$). In the case of a large disk eccentricity it is understandable that measuring the peak midpoint velocity as described in Section 3.2 would provide an inaccurate estimate of the systemic velocity. As such, we instead take the discrepancy between the gravitational redshifts as computed through the two different methods for Ton 345 as additional evidence for the large eccentricity of the gaseous disk ($e \sim 0.2 - 0.4$, Gänsicke *et al.* 2008a). It is noted that these high eccentricity values in Ton 345’s disk persist over long time-spans. Ton 345’s disk is likely pumped up to (and maintained at) high eccentricity by a surviving planet (Lubow 1991; Kley & Dirksen 2006).

6. Gas Disk Models

When observed at high spectral resolution the relatively clean-cut morphologies of the gaseous emission lines presented in Gänsicke *et al.* (2006, 2007, 2008a) resolve into complex structures. A common feature of the HIRES observed Ca II IRT emission lines for all three white dwarfs is a profile having the typical peak and wing structure (e.g., see Figure 1 in Horne & Marsh 1986) on one side of the emission (red side of the double peaked Ca II emission features for SDSS1228 and Ton 345 and the blue side for SDSS1043 in Figure 3) while having a peak with a sharp cut-off in emission (i.e., no wing) on the other side (blue side of the double peaked Ca II emission features for SDSS1228 and Ton 345 and the red side for SDSS1043 in Figure 3) of the emission. One could imagine that such an emission-line morphology would still be well reproduced by modeling the disks with families of elliptical rings as was done by Gänsicke *et al.* (2006, 2007, 2008a).

Werner *et al.* (2009) present a physical model to explain the gas emission lines observed in SDSS1228’s spectrum; their model relies on an active disk that is heated by viscous

dissipation of disk energy. We use the HIRES spectra to test the predictions of this model. In particular, we compare the HIRES spectra covering the Ca II H, K, and IRT transitions (Figure 3) to the predictions in Figure 6 of Werner *et al.* (2009). Werner *et al.* (2009) predict that the summed Ca II H & K emission complex should have flux that is a factor of ~ 5 stronger than the summed Ca II IRT flux. The Ca II H, K, and IRT emission lines detected in the spectra of SDSS1228 can be used as a robust test of the Werner *et al.* (2009) model. For each emission line the continuum flux is subtracted and the line flux summed. Extraction of the Ca II H emission line flux is not attempted as this complex is contaminated by the He ϵ absorption line. We instead assume that the emission line flux is the same for both of the Ca II H & K transitions and multiply the measured Ca II K emission line flux by 2 as a proxy for the sum of the emission line flux for both transitions. Examination of SDSS1228’s emission line flux for the Ca II H, K, and IRT transitions indicates that the summed Ca II H & K emission line flux is ~ 3.5 times weaker than the summed Ca II IRT emission line flux (see Table 9). Thus, the observational result differs by a factor of ~ 17 from that expected in the Werner *et al.* (2009) model. It is noted that the total flux in line emission is $\sim 3 \times 10^{-4}$ times the bolometric flux emitted by SDSS1228.

Assuming the line emission is optically thick (as is determined in the modeling presented in the supplemental material to Gänsicke *et al.* 2006), we can estimate the gas disk temperature from our observations by comparing the emission line flux for Ca II transitions in different parts of the optical spectrum. For SDSS1228, the only white dwarf with detected Ca II H+K emission, we estimate a gas disk temperature of ~ 5000 K. Gas disk temperature upper limits for Ton 345 and SDSS1043 are reported in Table 9.

6.1. Z II Region Model

The Werner *et al.* (2009) model does not provide a good match to the HIRES data. As such, we briefly describe an alternative model for the disk heating mechanism. We envision a model where the gas is photoionized by ultraviolet photons from the white dwarf. The idea would be akin to an H II region, but since this is a gas that is extremely deficient in H or He (Gänsicke *et al.* 2006, 2007, 2008a,b, and the results presented herein), it would be more aptly described as a Z II region. To determine the steady state temperature of a Z II region one must consider three processes:

- (i) injection of energy into the gas from photoionized electrons;
- (ii) energy loss from the gas when electrons recombine with ions, a process for Z II regions that would be negligible when compared to the last process:

- (iii) energy loss from the gas due to optically thick line emission. We assume that the gas density is sufficiently high ($\gg 10^6 \text{ cm}^{-3}$) that forbidden line cooling is unimportant and that gas instead cools through emission lines like the Ca II IRT.

We expect that the gas disk scale height will be significantly larger than the dust disk scale height (see Section 6.1.1). As a result, collisional energy transfer from gaseous atomic species to dust particles (e.g., Goldreich & Kwan 1974) will be negligible compared to the above three energy balance points. Hence, it is expected that the gas and dust temperatures are decoupled.

Here we provide details for a highly idealized Z II region model. We consider a flat passive disk (see Jura 2003b) whose thickness is a small fraction of the radius (R_*) of the illuminating star. The star is assumed to have effective temperature T_* and photospheric emission well described by a blackbody $B_\nu(T_*)$. At radial distance D from the star, we compute the effective disk-heating flux of stellar photons above energy threshold $h\nu_1$ with frequencies between ν_1 and ν_2 , $F^-(\nu_1, \nu_2)$ in the limit that $D \gg R_*$, as:

$$F^-(\nu_1, \nu_2) \approx \frac{2}{3} \left(\frac{R_*}{D} \right)^3 \left(\int_{\nu_1}^{\nu_2} \frac{B_\nu(T_*)}{h\nu} [h\nu - h\nu_1] d\nu \right) \quad (1)$$

If there is no gas in the system, then all the incident stellar flux heats the dust so that $\nu_1 = 0$ and $\nu_2 = \infty$. In a system with both dust and gas where, for simplicity, it is assumed that all gas atoms have the same average ionization potential $h\nu_I$, then the grains absorb all the photons with $\nu < \nu_I$ while the gas absorbs all the photons with $\nu > \nu_I$. Therefore, the flux heating the dust, F_{dust}^- , is computed from Equation (1) for $\nu_1 = 0$ and $\nu_2 = \nu_I$. Since we consider environments where $h\nu_I \gg kT_*$, most stellar photons are absorbed by grains, and the expected dust temperature is nearly the same as if no gas was present. For the flux heating the gas, F_{gas}^- , we use Equation (1) with $\nu_1 = \nu_I$ and $\nu_2 = \infty$. Using the Wien approximation for the Planck curve we find:

$$F_{gas}^- \approx \frac{2}{3} \left(\frac{R_*}{D} \right)^3 \frac{2h}{c^2} \left(\frac{kT_*}{h} \right)^4 \int_{x_I}^{\infty} (x^3 - x_I x^2) e^{-x} dx \quad (2)$$

where:

$$x_I = \frac{h\nu_I}{kT_*}. \quad (3)$$

From expressions (1) and (2), we find:

$$\frac{F_{gas}^-}{F_{dust}^-} \approx \frac{(x_I^2 + 4x_I + 6)e^{-x_I}}{\pi^4/15}. \quad (4)$$

The value of $h\nu_I$ is determined from the metallic constituents in a gaseous disk. Hence, knowledge of the gas disk composition is imperative in calculating this average energy of a photoelectron and the distribution of its energy into the gaseous material. Gänsicke *et al.* (2006, 2007, 2008a) report emission lines from Ca in all three white dwarfs and Fe in SDSS1228 and Ton 345, absorption lines of Mg in all three white dwarfs, and Ca and Si absorption in Ton 345. Under the assumption that heavy elements in the photospheres of these white dwarfs were accreted from their disks (see e.g., Zuckerman *et al.* 2007; Klein *et al.* 2010), we can claim that each gas disk holds at least the elements Mg, Fe, Si, and Ca. With this mix of elements we calculate an average ionizing potential of ~ 8 eV. Better knowledge of the gas disk composition, and ultimately the energetics of the gas disk, is most likely to come from deep, high-spectral resolution spectroscopic observations of these white dwarfs in the ultraviolet. For the case of a star with effective temperature $T_* = 20,000$ K and $h\nu_I = 8$ eV, we compute $F_{gas}^-/F_{dust}^- \approx 5\%$.

From the measurements reported in Table 9 for SDSS1228, Ton 345, and SDSS1043 we see that the line fluxes received at Earth summed over the calcium triplet emission are roughly 10×10^{-15} , 4×10^{-15} , and 2×10^{-15} erg cm $^{-2}$ s $^{-1}$, respectively. For these same three stars, the fluxes from the dust can be very roughly approximated as νF_ν evaluated at $3.6 \mu\text{m}$, or 2×10^{-13} , 2×10^{-13} , and 3×10^{-14} erg cm $^{-2}$ s $^{-1}$. Therefore, for each of the three white dwarfs, the ratio of the flux received in the calcium triplet line emission compared to the flux received from the dust is $\sim 5\%$, as predicted. We take this agreement of the data with the model as support of our description of the systems as Z II regions.

The flux re-radiated by the gas in the disk, F_{gas}^+ is:

$$F_{gas}^+ = \sum \pi B_\nu(T_{gas}) \Delta\nu \quad (5)$$

In this expression, the sum is performed over all important cooling lines, here assumed to be the three members of the calcium triplet. Although the disk is orbiting rapidly, we assume that each portion of the gas is in vertical hydrostatic equilibrium and that the local microscopic gas motions are mainly thermal. Therefore:

$$\Delta\nu = \beta_{line} \left(\frac{2kT_{gas}}{m(Ca)} \right)^{1/2} \frac{\nu_L}{c} \quad (6)$$

where ν_L is the line frequency, $m(Ca)$ is the mean atomic weight of calcium, and β_{line} is a coefficient of order unity. We compute the gas temperature by finding the value of T_{gas} such that:

$$F_{gas}^+(T_{gas}) = F_{gas}^-. \quad (7)$$

With considerable simplifications, we compute an analytic solution to Equation (6). We assign the same frequency to all three members of the calcium triplet and take $\beta_{line} = 4$. Combining the previous equations we find:

$$F_{gas}^+ \approx 12 \left(\frac{2 k T_{gas}}{m(Ca)} \right)^{1/2} \frac{2 \pi h \nu_L^4}{c^3} e^{-h\nu_L/kT_{gas}}. \quad (8)$$

For convenience, we define A such that:

$$A = \frac{1}{18 \pi} \left(\frac{R_*}{D} \right)^3 c \left(\frac{m(Ca)}{2 k T_{gas}} \right)^{1/2} \left(\frac{\nu_*}{\nu_L} \right)^4 (x_I^2 + 4 x_I + 6) \quad (9)$$

where $h\nu_* = k T_*$. Combining the above equations, we find:

$$T_{gas}(D) = T_* \left(\frac{\nu_I}{\nu_L} - \frac{\nu_*}{\nu_L} \ln A \right)^{-1}. \quad (10)$$

Gas temperatures are calculated as a function of distance from the star using the analytic solution in Equation (10) and are plotted for specific cases in Figure 9. We assume in these calculations that $m(Ca) = 40$ atomic mass units. For $D \ll 20 R_*$, the simple model fails because there is insufficient cooling. However, for $D \gg R_*$ and $T_{eff} = 20,000$ K, we see that the gas temperature ranges from 6000 K to 3000 K, depending upon the exact distance from the star. Such gas disk temperatures are roughly in agreement with those estimated from observations of the three gas disk-hosting stars.

6.1.1. Decoupled Gas and Dust Disks

In our scenario for tidally-disrupted disks orbiting white dwarfs, the gas temperature and the dust temperature are distinct because the gas and dust are spatially separated. The dust is assumed to be confined to a flat disk somewhat analogous to Saturn’s ring. Depending upon the mass of the tidally-disrupted rocky object and the extent of the radial zone where

the material is located, the vertical thickness of the dust may be only 1 cm. In contrast, the gas is pictured to be in vertical hydrostatic equilibrium and therefore:

$$\rho_{gas} = \rho(0) e^{-z^2/H^2} \quad (11)$$

where $\rho(0)$ is the midplane density. For gas orbiting at radial distance D from the star of mass M_* :

$$H = \left(\frac{2 k T_{gas} D^3}{G M_* \mu} \right)^{1/2}. \quad (12)$$

With $D = 10^{10}$ cm, $T_{gas} \sim 6,000$ K, $M_* = 0.6 M_\odot$, and adopting $\mu = 2.4 \times 10^{-23}$ g as representative of an ionized gas of heavy atoms, we estimate $H \approx 3 \times 10^7$ cm. Thus, the bulk of the gas is very far from the dust and their temperatures may be different.

7. Discussion

From the imaging and spectroscopic data we have estimated inner and outer radii for both the gas and dust disks using as few assumptions as possible to connect the dust and gas disk results. Now, the two disk parameter sets are combined to understand how the gas and dust are related, and what that can tell one about their origin and evolution.

Dust disk inner radii are close to what is expected to correspond to the sublimation temperature for silicate dust particles. Spitzer IRS observations presented in Jura *et al.* (2009) suggest white dwarfs with circumstellar disks have orbiting dust composed of olivine. The limited wavelength coverage of these spectra preclude more complete compositional analyses (but see Reach *et al.* 2009). None of the gas disk-hosting white dwarfs discussed herein have existing mid-infrared spectroscopic observations, hence there is some uncertainty in what dust species orbit these three white dwarf stars and at what temperature these materials will sublimate. The dust outer disk radius for SDSS1228 is consistent with the expectation for its Roche radius and in light of similar results for several other dust disk-hosting white dwarfs (e.g., Farihi *et al.* 2009), we assume the same is true for Ton 345 and SDSS1043.

Gas disk outer radii are spatially coincident (to within measured and modeled uncertainties) with dust disk outer radii (Figure 8). The gas disk inner radius for SDSS1228 and Ton 345 appears to be farther from the host star than the dust disk inner radius. For SDSS1043 the gas disk is closer to the host star, although the uncertainty range for its gas disk inner

radius is large (Table 8). Slightly different disk inclinations (that are still within the range of viable model parameters, see Table 7) could push the dust and gas disk inner radii into better agreement. Lower disk inclination values than those quoted in Table 7 would result in gas disk inner radii closer to the host white dwarf star and dust disk inner radii farther away from the host white dwarf star and vice-versa.

Similar outer radii of the dusty and gaseous disks for the three white dwarfs can be understood through the formalism developed in Jura (2008). Jura (2008) suggests that pre-existing dusty disk material can sputter entering rocky object material from a white dwarf’s remnant planetary system. The pre-existing material would have been some rocky material that was tidally shredded after falling within the white dwarf’s tidal radius. New infalling material would tidally shred and then sputter out onto the pre-existing disk, populating the disk with gaseous material. Steady state flows of rocky material could maintain the dusty and gaseous disks that are observed around each of the three white dwarfs.

The above discussion of disk inner radii suggests that the gas and dust disks are likely to be entirely spatially coincident from inner to outer disk. However, the best fit model parameters (Table 7) for SDSS1228’s and Ton 345’s disk systems would have to be stretched to the extremes of their viable ranges to be in agreement. Here we discuss another possible way that the dust disks around SDSS1228 and Ton 345 could reside farther from the host stars and be more in agreement with the gas disk inner radii without changing disk inclination angles. Flat dust disk models predict the temperatures shown in Table 7. As suggested by Brinkworth *et al.* (2009), if a warp were present in a dust disk then its grains could be cooler and located farther from their host white dwarf star while still reproducing the observed excess infrared emission. Warps for the dust disk-hosting white dwarfs GD 362 and GD 56 have been suggested by Jura *et al.* (2007b, 2009). A slight warp in the dust disk of SDSS1228 or Ton 345 could inflate the inner radius by a factor $\gtrsim 1$ (Jura *et al.* 2009). Such an inflation could bring SDSS1228’s and Ton 345’s inner dust disk radii into agreement with their inner gas disk radii. For the case of SDSS1043, the combined uncertainties for its gas and dust disk inner radii are compatible with both terminating at the same inner radius. The asymmetric gas emission lines observed (Figure 3) suggest that the white dwarfs’ gas disks are not likely to be flat, lending support to a warped dust disk interpretation.

Increased disk viscosity at the gas and dust disk inner termination radius can provide an explanation for similar gas and dust disk inner radii as well as the lack of emission corresponding to material extending inwards to the white dwarf stars. In the region of the disk where dust grains are not yet sublimated, the net viscosity of the disk is small and disk material does not drift inwards rapidly. The inner disk is heated to the sublimation temperature where grains begin to vaporize resulting in inner disk material that is all gaseous

and ionized. Higher densities of hot gas leads to enhanced disk viscosity which causes material to drift inwards towards the host white dwarf star on short timescales. Rapid inner disk depletion will result in small values of inner disk surface density, consistent with the lack of any emission having velocities corresponding to radii closer to the white dwarf than the observed inner disk radii. Thus, the sublimation of dust grains and resulting enhanced gas density can potentially explain coincident gas and dust disk inner radii around these white dwarfs. The eventual fate of the inner disk material will be to accrete onto the host white dwarf star, polluting its atmosphere and providing a unique insight into its bulk composition (e.g., Zuckerman *et al.* 2007; Klein *et al.* 2010; Dufour *et al.* 2010).

8. Conclusion

We have obtained a suite of ground-based optical and near-infrared measurements of three gas-disk hosting white dwarfs. Unambiguous infrared excess emission is identified towards Ton 345, confirming that this white dwarf hosts a dusty disk in addition to its gaseous disk. Characterization of these three gaseous and dusty disk systems indicates that the gas and dust disks are spatially coincident at their outer radii and likely their inner radii. Disk parameterization results are consistent with a scenario where both dust and gas disks have their origin in the dissolution of rocky objects from the white dwarfs’ remnant planetary systems.

Detection of the Ca II H & K and Ca II IRT lines in emission towards SDSS1228 enables the development of a new model for the gas disk heating mechanism. This model relies on photoionization of metallic atoms in a metal-dominated region around the hot white dwarfs and cooling of the gaseous material through optically thick emission lines.

C.M. acknowledges support from the Spitzer Visiting Graduate Student program and from a LLNL Minigrant to UCLA. We would like to thank the observers and queue coordinators who carried out service observations at CFHT (programs 08AD96). We thank Detlev Koester for providing atmospheric models for SDSS1228 and SDSS1043 and Jay Farihi for helpful discussion. We thank Carolyn Brinkworth for useful discussion and for allowing us to use unpublished Spitzer results for SDSS1043. Based on observations obtained with WIRCam, a joint project of CFHT, Taiwan, Korea, Canada, France, at the Canada-France-Hawaii Telescope (CFHT) which is operated by the National Research Council (NRC) of Canada, the Institut National des Sciences de l’Univers of the Centre National de la Recherche Scientifique of France, and the University of Hawaii. Based on observations obtained at the Gemini Observatory, which is operated by the Association of Universities

for Research in Astronomy, Inc., under a cooperative agreement with the NSF on behalf of the Gemini partnership: the National Science Foundation (United States), the Science and Technology Facilities Council (United Kingdom), the National Research Council (Canada), CONICYT (Chile), the Australian Research Council (Australia), Ministério da Ciência e Tecnologia (Brazil) and Ministerio de Ciencia, Tecnología e Innovación Productiva (Argentina). We are grateful to the Director of the Gemini North telescope for granting us observing time. Some of the data presented herein were obtained at the W.M. Keck Observatory, which is operated as a scientific partnership among the California Institute of Technology, the University of California and the National Aeronautics and Space Administration. The Observatory was made possible by the generous financial support of the W.M. Keck Foundation. This publication makes use of data products from the Two Micron All Sky Survey, which is a joint project of the University of Massachusetts and the Infrared Processing and Analysis Center/California Institute of Technology, funded by the National Aeronautics and Space Administration and the National Science Foundation. Funding for the SDSS and SDSS-II has been provided by the Alfred P. Sloan Foundation, the Participating Institutions, the National Science Foundation, the U.S. Department of Energy, the National Aeronautics and Space Administration, the Japanese Monbukagakusho, the Max Planck Society, and the Higher Education Funding Council for England. Based on observations made with the NASA Galaxy Evolution Explorer. GALEX is operated for NASA by the California Institute of Technology under NASA contract NAS5-98034. This research was supported in part by NASA and NSF grants to UCLA.

Facilities: CFHT (WIRCam), Gemini:North (NIRI), Keck:I (HIRES), Shane (Gemini)

REFERENCES

- Abazajian, K. N., *et al.* 2009, *ApJS*, **182**, 543
- Albert, C. E., Blades, J. C., Morton, D. C., Lockman, F. J., Proulx, M., & Ferrarese, L. 1993, *ApJS*, **88**, 81
- Becklin, E. E., Farihi, J., Jura, M., Song, I., Weinberger, A. J., & Zuckerman, B. 2005, *ApJ*, **632**, L119
- Bertin, E. 2006, in *Astronomical Data Analysis Software and Systems XV*, edited by C. Gabriel, C. Arviset, D. Ponz, & S. Enrique, vol. 351 of *Astronomical Society of the Pacific Conference Series*, 112–+
- Bertin, E. & Arnouts, S. 1996, *A&AS*, **117**, 393

- Brinkworth, C. S., Gänsicke, B. T., Marsh, T. R., Hoard, D. W., & Tappert, C. 2009, *ApJ*, **696**, 1402
- Burleigh, M. R., Clarke, F. J., & Hodgkin, S. T. 2002, *MNRAS*, **331**, L41
- Cardelli, J. A., Clayton, G. C., & Mathis, J. S. 1989, *ApJ*, **345**, 245
- Cutri, R. M., *et al.* 2003, *2MASS All Sky Catalog of point sources.*, The IRSA 2MASS All-Sky Point Source Catalog, NASA/IPAC Infrared Science Archive. <http://irsa.ipac.caltech.edu/applications/Gator/>
- Davidsson, B. J. R. 1999, *Icarus*, **142**, 525
- Debes, J. H. & Sigurdsson, S. 2002, *ApJ*, **572**, 556
- Dufour, P., Kilic, M., Fontaine, G., Bergeron, P., Lachapelle, F., Kleinman, S. J., & Leggett, S. K. 2010, *ArXiv e-prints*
- Duncan, M. J. & Lissauer, J. J. 1998, *Icarus*, **134**, 303
- Farihi, J., Jura, M., Lee, J., & Zuckerman, B. 2010, *ApJ*, **714**, 1386
- Farihi, J., Jura, M., & Zuckerman, B. 2009, *ApJ*, **694**, 805
- Gänsicke, B. T., Koester, D., Marsh, T. R., Rebassa-Mansergas, A., & Southworth, J. 2008a, *MNRAS*, **391**, L103
- Gänsicke, B. T., Marsh, T. R., & Southworth, J. 2007, *MNRAS*, **380**, L35
- Gänsicke, B. T., Marsh, T. R., Southworth, J., & Rebassa-Mansergas, A. 2006, *Science*, **314**, 1908
- 2008b, in *Astronomical Society of the Pacific Conference Series*, edited by D. Fischer, F. A. Rasio, S. E. Thorsett, & A. Wolszczan, vol. 398 of *Astronomical Society of the Pacific Conference Series*, 149–+
- Goldreich, P. & Kwan, J. 1974, *ApJ*, **189**, 441
- Graham, J. R., Matthews, K., Neugebauer, G., & Soifer, B. T. 1990, *ApJ*, **357**, 216
- Hodapp, K. W., *et al.* 2003, *PASP*, **115**, 1388
- Hogan, E., Burleigh, M. R., & Clarke, F. J. 2009, *MNRAS*, 727
- Holsapple, K. A. & Michel, P. 2008, *Icarus*, **193**, 283

- Horne, K. & Marsh, T. R. 1986, *MNRAS*, **218**, 761
- Jura, M. 2003a, *ApJ*, **582**, 1032
- 2003b, *ApJ*, **584**, L91
- 2008, *AJ*, **135**, 1785
- Jura, M., Farihi, J., & Zuckerman, B. 2007a, *ApJ*, **663**, 1285
- 2009, *AJ*, **137**, 3191
- Jura, M., Farihi, J., Zuckerman, B., & Becklin, E. E. 2007b, *AJ*, **133**, 1927
- Kilic, M. & Redfield, S. 2007, *ApJ*, **660**, 641
- Kilic, M., von Hippel, T., Leggett, S. K., & Winget, D. E. 2005, *ApJ*, **632**, L115
- 2006, *ApJ*, **646**, 474
- Klein, B., Jura, M., Koester, D., Zuckerman, B., & Melis, C. 2010, *ApJ*, **709**, 950
- Kley, W. & Dirksen, G. 2006, *A&A*, **447**, 369
- Krivov, A. V. 2010, *Research in Astronomy and Astrophysics*, **10**, 383
- Lubow, S. H. 1991, *ApJ*, **381**, 259
- McLean, I. S., *et al.* 1993, in *Society of Photo-Optical Instrumentation Engineers (SPIE) Conference Series*, edited by A. M. Fowler, vol. 1946 of *Presented at the Society of Photo-Optical Instrumentation Engineers (SPIE) Conference*, 513–533
- Morrissey, P., *et al.* 2007, *ApJS*, **173**, 682
- Mullally, F., Reach, W. T., Degennaro, S., & Burrows, A. 2009, *ApJ*, **694**, 327
- Mullally, F., Winget, D. E., Degennaro, S., Jeffery, E., Thompson, S. E., Chandler, D., & Kepler, S. O. 2008, *ApJ*, **676**, 573
- Puget, P., *et al.* 2004, in *Society of Photo-Optical Instrumentation Engineers (SPIE) Conference Series*, edited by A. F. M. Moorwood & M. Iye, vol. 5492 of *Society of Photo-Optical Instrumentation Engineers (SPIE) Conference Series*, 978–987
- Reach, W. T., Kuchner, M. J., von Hippel, T., Burrows, A., Mullally, F., Kilic, M., & Winget, D. E. 2005, *ApJ*, **635**, L161

- Reach, W. T., Lisse, C., von Hippel, T., & Mullally, F. 2009, *ApJ*, **693**, 697
- Sackmann, I.-J., Boothroyd, A. I., & Kraemer, K. E. 1993, *ApJ*, **418**, 457
- Sanders, D. B., *et al.* 2007, *ApJS*, **172**, 86
- Tokunaga, A. T., Becklin, E. E., & Zuckerman, B. 1990, *ApJ*, **358**, L21
- Vogt, S. S., *et al.* 1994, in *Proc. SPIE Instrumentation in Astronomy VIII, David L. Crawford; Eric R. Craine; Eds., Volume 2198, p. 362*, edited by D. L. Crawford & E. R. Craine, vol. 2198 of *Presented at the Society of Photo-Optical Instrumentation Engineers (SPIE) Conference*, 362
- Werner, K., Nagel, T., & Rauch, T. 2009, *Journal of Physics Conference Series*, **172**, 012054
- Werner, M. W., *et al.* 2004, *ApJS*, **154**, 1
- York, D. G., *et al.* 2000, *AJ*, **120**, 1579
- Zacharias, N., Monet, D. G., Levine, S. E., Urban, S. E., Gaume, R., & Wycoff, G. L. 2004, in *Bulletin of the American Astronomical Society*, vol. 36 of *Bulletin of the American Astronomical Society*, 1418–+
- Zuckerman, B. & Becklin, E. E. 1987, *Nature*, **330**, 138
- Zuckerman, B., Koester, D., Melis, C., Hansen, B. M., & Jura, M. 2007, *ApJ*, **671**, 872
- Zuckerman, B. & Song, I. 2004, *ApJ*, **603**, 738

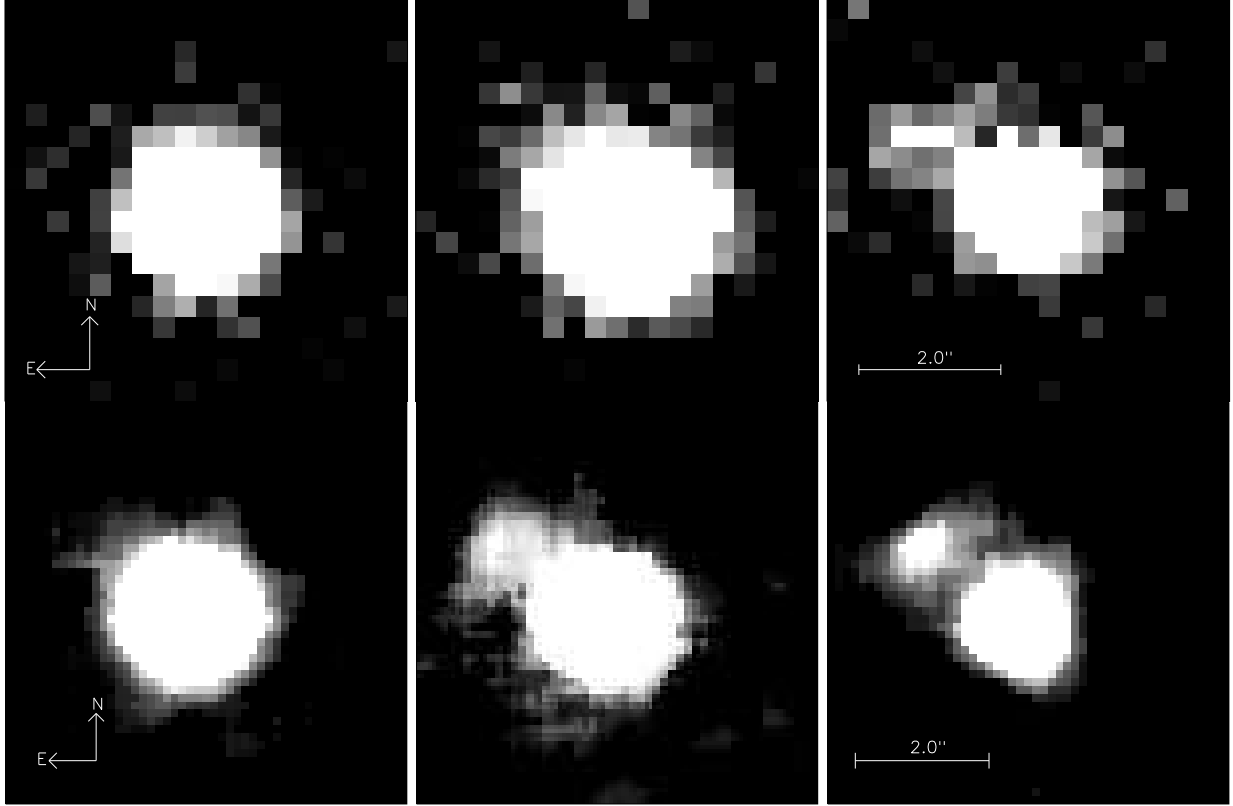


Fig. 1.— *Top panels*: CFHT WIRCam images of Ton 345 in the J-, H-, and K_s-bands (from left to right) with a linear stretch. The image orientation and scale is the same for all three bands. Note the fainter source located $\sim 2.0''$ to the NE of Ton 345. This faint background source does not contribute a significant amount of flux to the CFHT measured magnitudes of Ton 345. *Bottom panels*: Gemini North NIRI images of Ton 345 in the J-, H-, and K_s-bands (from left to right) presented on a linear stretch. Images were smoothed over with a 7-pixel boxcar to enhance the faint background object contrast. The image orientation and scale is the same for all three bands. The background source, presumably a galaxy, is now clearly detected in the H- and K_s-bands.

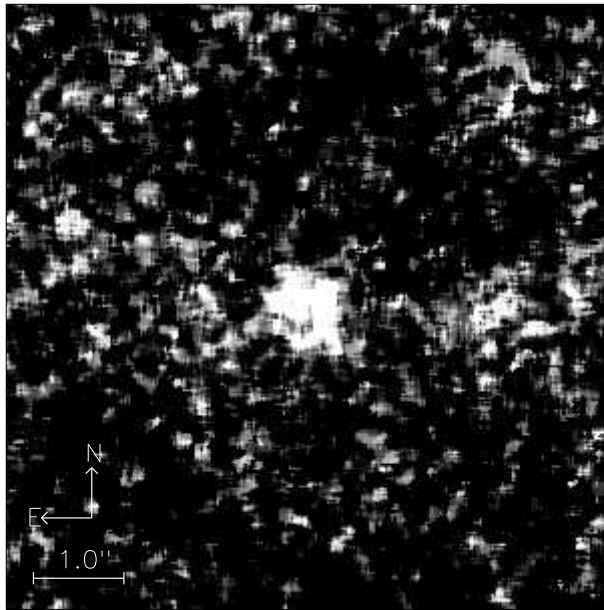


Fig. 2.— Gemini North NIRI image of Ton 345 in the L' -band presented on a linear stretch after being smoothed over with a 7-pixel boxcar. The fluctuations in the background around Ton 345 are representative of the 1σ noise level. The background galaxy is not detected, it is likely too diffuse for the sensitivity threshold of this imaging set.

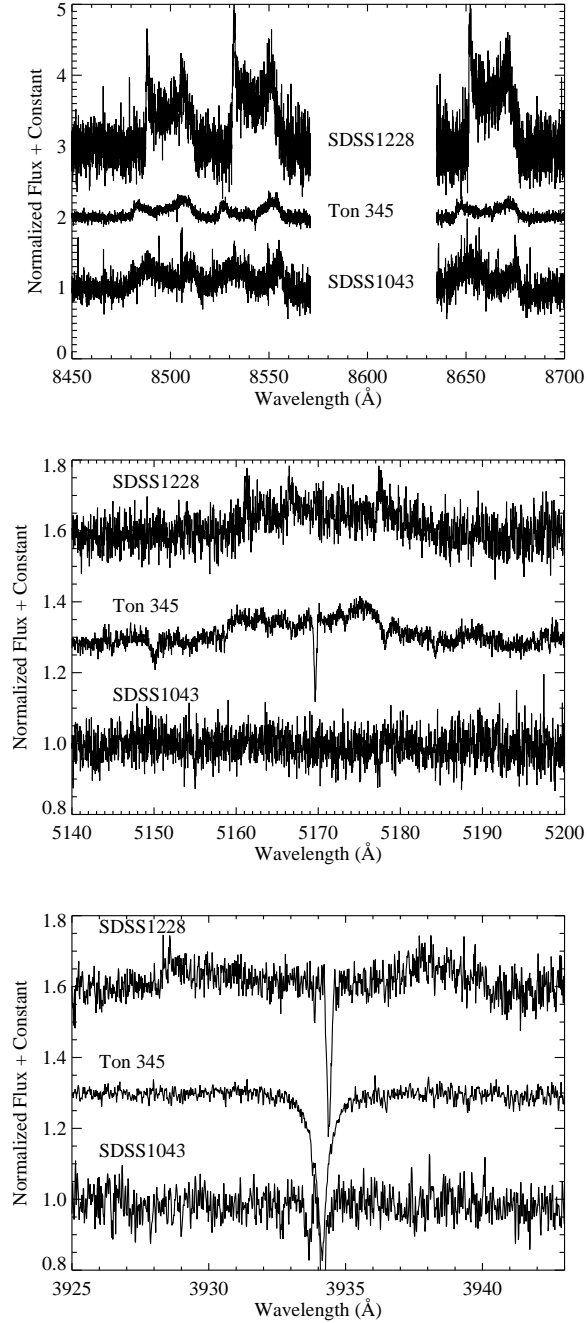


Fig. 3.— Gas emission lines detected in HRES optical spectra for SDSS1228, Ton 345, and SDSS1043. *Top Panel:* Ca II infrared triplet region. Combined spectra from the 2008 November run are plotted. The lack of data around ~ 8600 Å is due to the gap between red orders for the HRES setup used. *Middle Panel:* Fe II $\lambda 5169$ region. Combined spectra from the 2008 November run are plotted. Emission lines are seen only in SDSS1228 and Ton 345. SDSS1228 appears to have three emission peaks where one may be due to emission from one of the Mg I b triplet transitions. *Bottom Panel:* Ca II K region. Plotted spectra are from the 2007 May run for SDSS1228 and SDSS1043, and from the 2008 February run for Ton 345. Emission lines are seen only in SDSS1228 (Ca II H emission for SDSS1228 is detected but not shown). The weak, blueshifted Ca II absorption components are likely interstellar in nature based on comparison to known interstellar Ca II K line strengths and velocities in the direction towards each white dwarf (Albert *et al.* 1993). Wavelengths in this figure are corrected to the heliocentric reference frame and are presented in air.

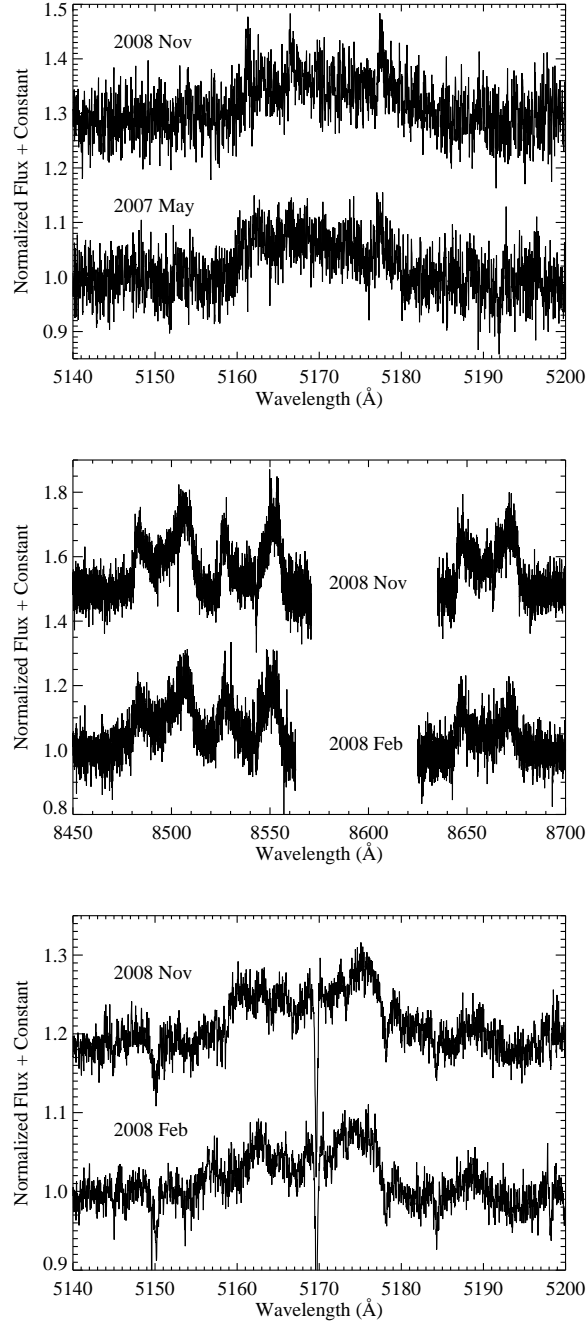


Fig. 4.— Multiple epochs of gas emission lines detected in the HIRES spectra. *Top Panel:* Fe II $\lambda 5169$ emission lines for SDSS1228. The 2007 May data are from a single exposure. The 2008 Nov data are three combined exposures. The S/N of each are roughly equivalent (see Table 4). The relative strength of the three emission peaks seems to vary between the two epochs, although the S/N of each epoch prevents any conclusive analysis. *Middle Panel:* Ca II infrared triplet emission lines for Ton 345. All measurable parameters for the two epochs agree to within their respective errors. *Bottom Panel:* Fe II $\lambda 5169$ emission lines for Ton 345. All measurable parameters for the two epochs agree to within their respective errors. Wavelengths in this figure are corrected to the heliocentric reference frame and are presented in air.

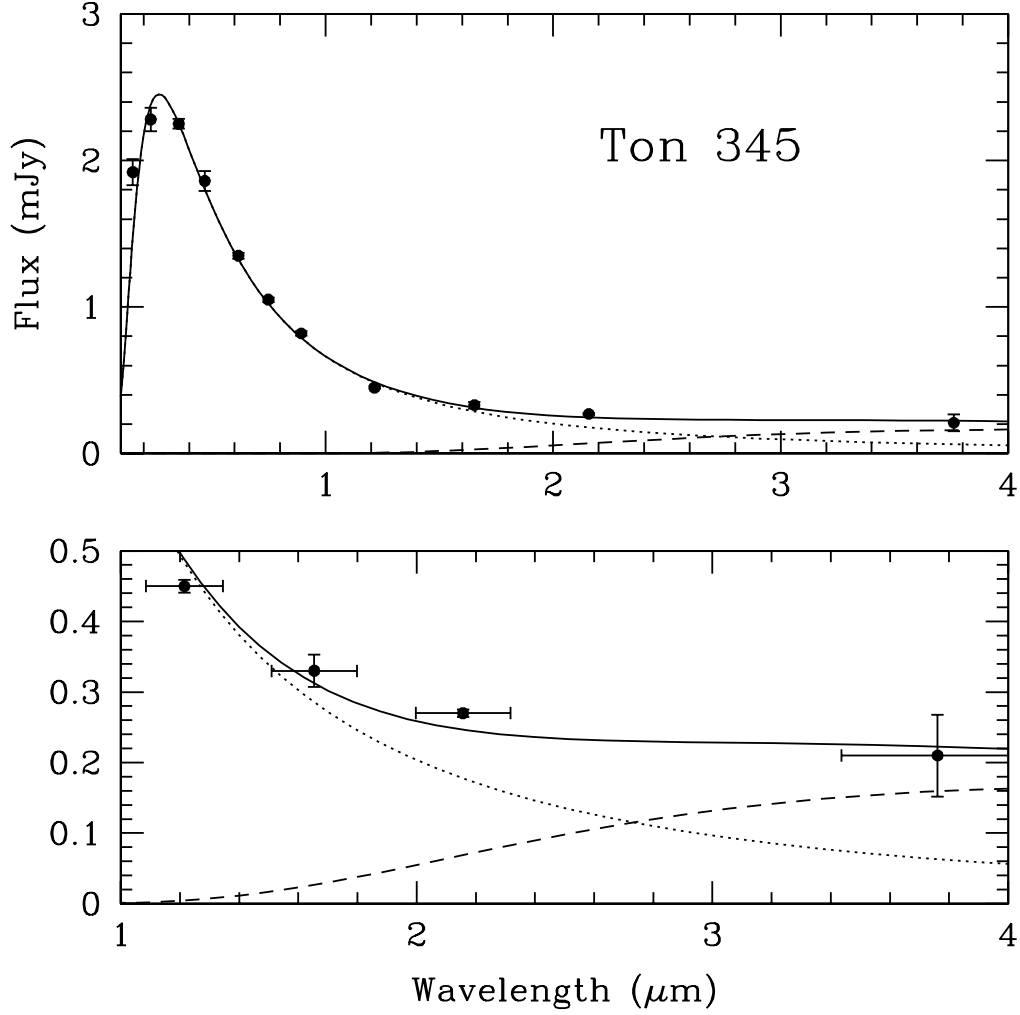


Fig. 5.— SED for the DBZ white dwarf Ton 345. Overplotted is a model for the white dwarf photospheric emission (a blackbody with $T_{\text{eff}} \sim 18,600$ K represented by the dotted line) and an orbiting flat, passive, opaque dust disk (represented by the dashed line). Broad-band fluxes can be found in Table 1 and the model parameters can be found in Table 7. Horizontal bars correspond to filter bandpasses. Optical fluxes were obtained from SDSS while ultraviolet fluxes were taken from the GALEX AIS and MIS catalogs. K_s and L' are in excess of what one would expect from the photosphere of the white dwarf alone.

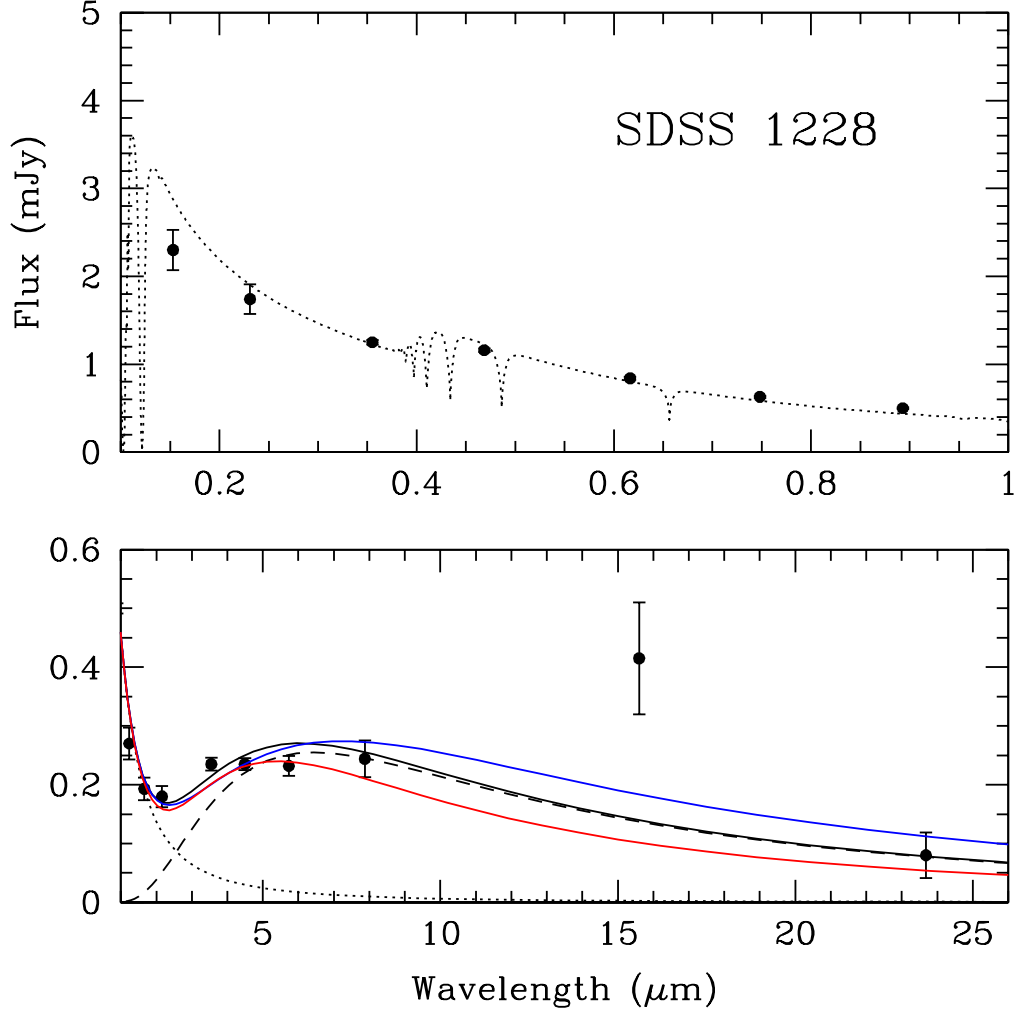


Fig. 6.— SED for the DAZ white dwarf SDSS1228. Overplotted are models for an atmosphere of a $T_{\text{eff}}=22,020$ K, $\log(g)=8.24$, DA white dwarf (dotted line; D. Koester, 2009 private communication) with an orbiting flat, passive, opaque dust disk (dashed line). Input infrared fluxes are taken from Brinkworth *et al.* (2009). Three different disk models are displayed to illustrate a range of viable model parameters. The black model curve (the middle of the three) is the best fit and the model whose parameters we adopt for SDSS1228’s dusty disk (see Table 7). Optical fluxes were obtained from SDSS while ultraviolet fluxes were taken from the GALEX AIS catalog. One possible explanation for the relatively high flux at $16 \mu\text{m}$ is that the source possesses a strong silicate emission feature (Brinkworth *et al.* 2009), thus it is not included in the continuum fit.

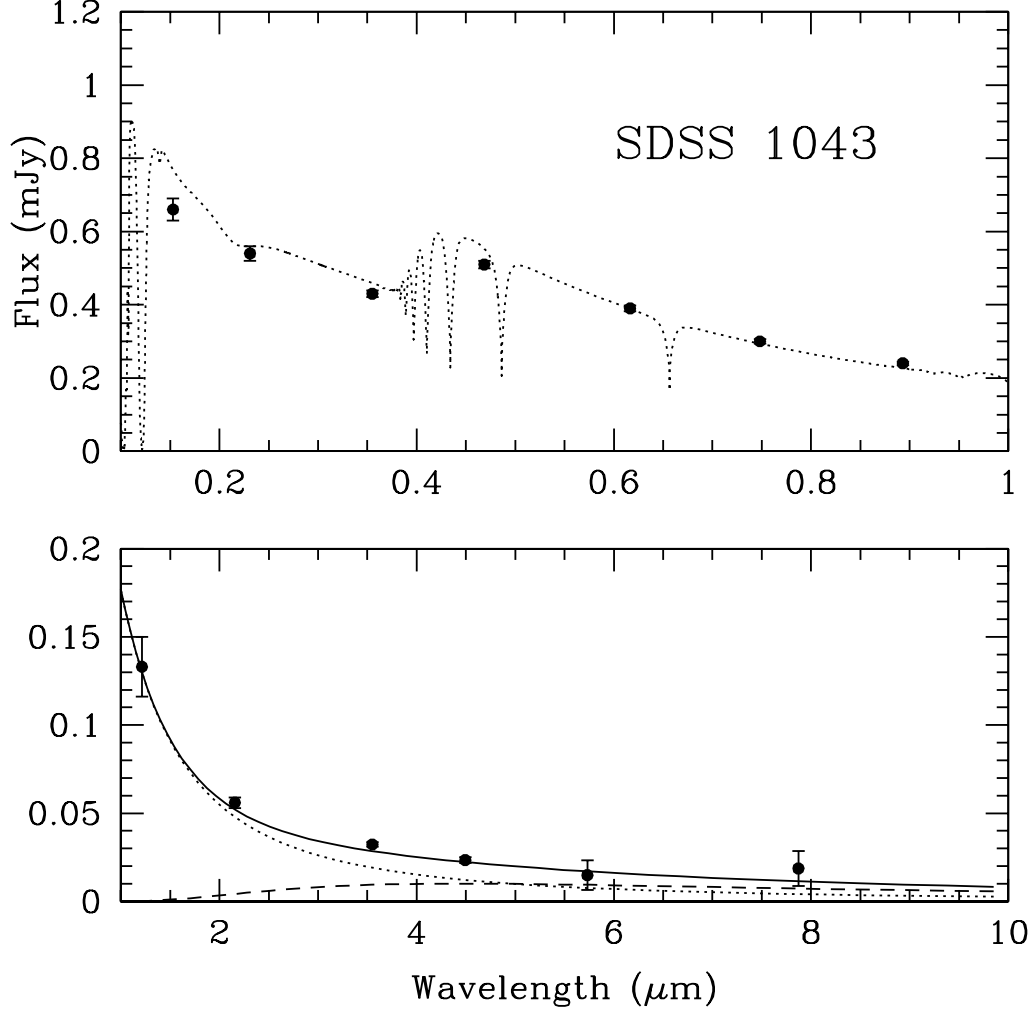


Fig. 7.— SED for the DAZ white dwarf SDSS1043. Overplotted is a model atmosphere for a $T_{\text{eff}}=18,330$ K, $\log(g)=8.09$, DA white dwarf (dotted line; D. Koester, 2009 private communication) with an orbiting flat, passive, opaque dust disk (dashed line). The model UV fluxes are reddened using the Cardelli *et al.* (1989) extinction curve assuming $E(B-V)=0.03$. Fluxes can be found in Table 2 and the model parameters are presented in Table 7. Data points longward of $2 \mu\text{m}$ are IRAC measurements reported in C. Brinkworth *et al.* (2010, in preparation). Optical fluxes were obtained from SDSS while ultraviolet fluxes were obtained from the GALEX AIS catalog. When plotted with the Spitzer IRAC data, the K_s measurement suggests an excess beginning at $\sim 2 \mu\text{m}$.

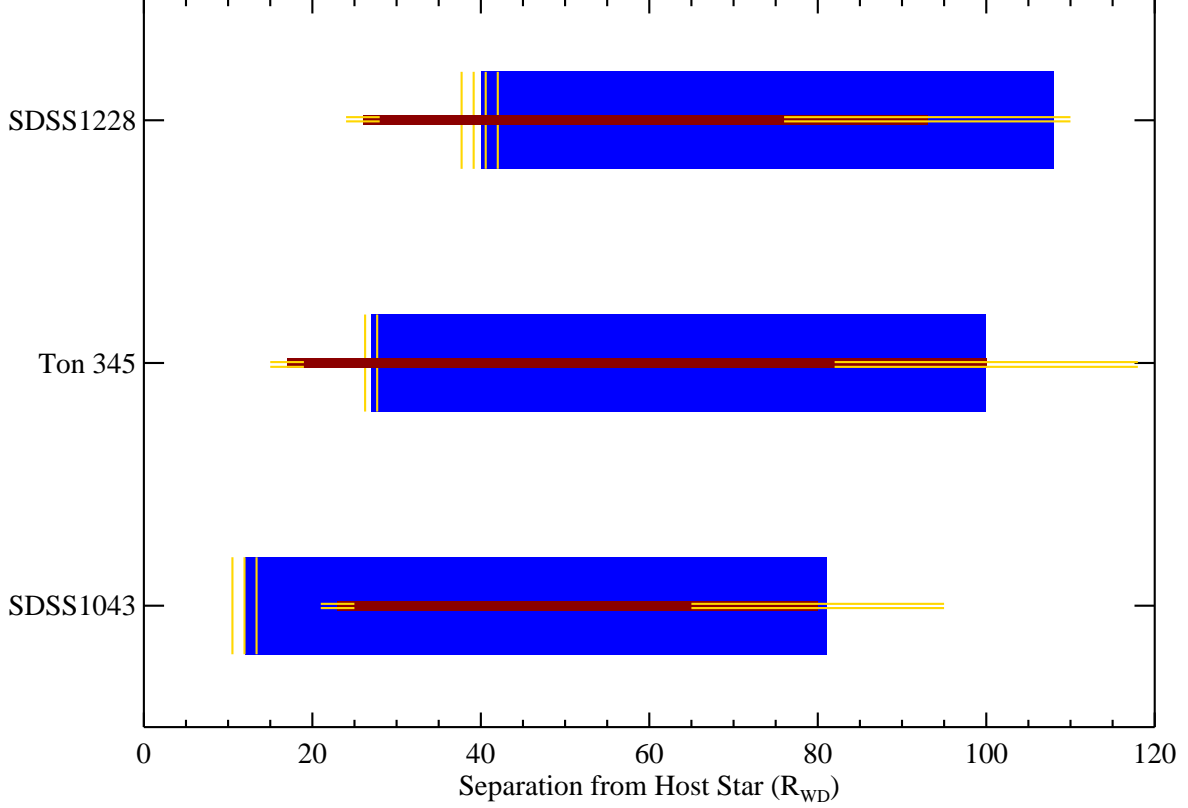


Fig. 8.— Sketch illustrating the results presented in Table 8. The dimensions of each white dwarf’s dusty and gaseous disks are plotted in units of each white dwarf’s radius. True blue colored regions correspond to gas disks while cardinal red colored regions correspond to dust disks. The vertical scale heights of the gas disks are expected to be larger than those of the dust disks (Section 6.1.1). Gold, horizontally hatched regions correspond to the 1σ uncertainty for the dust disk inner and outer radii as reported in Table 8. Gold, vertically hatched regions correspond to the 1σ uncertainty for the gas disk inner radii as reported in Table 8.

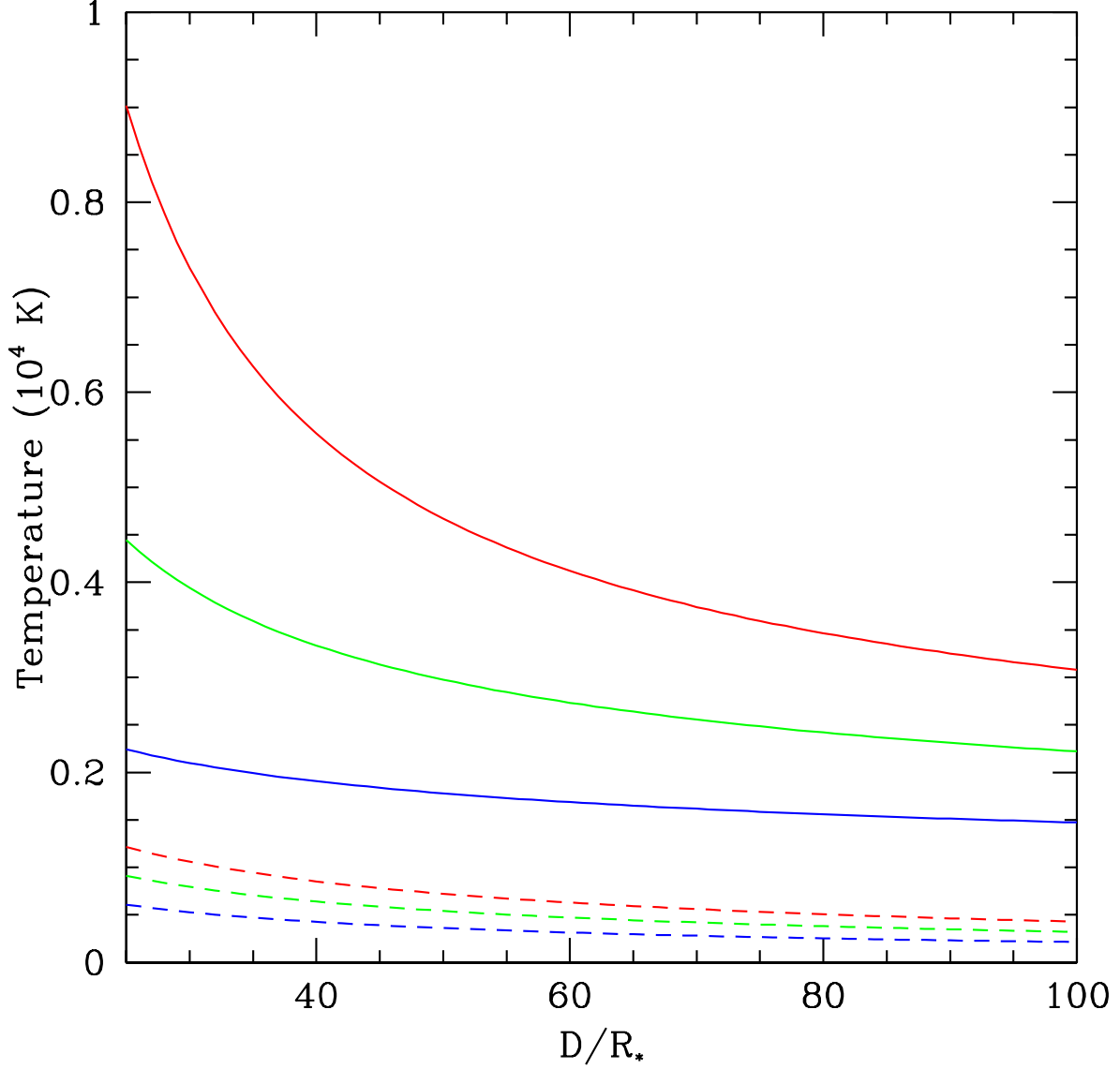


Fig. 9.— Disk temperature as a function of radial separation from its host white dwarf star in units of stellar radii. The solid lines are for the gas disk temperature as calculated using the analytical Z II region model outlined in Section 6.1. Dashed lines are dust disk temperatures as described in Section 4. The red, green, and blue curves are for stellar effective temperatures of 20,000 K, 15,000 K, and 10,000 K respectively. We note that the gas disk model predictions fail for $D/R_* < 20$ (see Section 6.1).

Table 1. Broad-band Fluxes for Ton 345

Band	λ nm	mag			Flux Density (mJy)		
		NIR					
		WIRCam ^b	NIRI ^b	Average	F _{obs}	F _* ^a	F _{excess}
L'	3761	—	15.2±0.3	—	0.21±28%	0.075	0.135±0.059
K _s	2157	15.95±0.03	16.04±0.03	15.99±0.02	0.27±2%	0.19	0.076±0.005
H	1654	16.18±0.05	16.33±0.02	16.26±0.07	0.33±7%	0.29	0.036±0.023
J	1215	16.36±0.03	16.41±0.03	16.39±0.02	0.45±2%	0.45	0.00
SDSS DR7— Optical							
<i>z</i>	893.1	16.615±0.018				0.82±1.8%	
<i>i</i>	748.1	16.348±0.015				1.05±1.5%	
<i>r</i>	616.5	16.077±0.014				1.35±1.4%	
<i>g</i>	468.6	15.728±0.035				1.86±3.5%	
<i>u</i>	355.1	15.559±0.015				2.25±1.5%	
GALEX ^b — Ultraviolet							
NUV	227.1	15.50±0.03				2.28±3%	
FUV	152.8	15.69±0.05				1.92±5%	

^aF_{*} is the predicted photospheric flux density in the given bandpass assuming Ton 345 is a blackbody with T_{eff} of 18,600 K and that the J-band monochromatic flux is entirely photospheric in nature.

^bWIRCam and NIRI magnitudes are in the Johnson system. GALEX measurements are in AB magnitudes. GALEX uncertainties are as suggested in Morrissey *et al.* (2007).

Table 2. Broad-band Fluxes for SDSS1043

Band	λ nm	mag	F_{obs} (mJy)
WIRCam/Gemini ^{a,b} – NIR			
K _s	2157	17.69±0.05	0.056±5%
J	1210	17.72±0.14	0.133±13%
SDSS DR7 – Optical			
<i>z</i>	893.1	17.942±0.036	0.24±3.6%
<i>i</i>	748.1	17.701±0.017	0.30±1.7%
<i>r</i>	616.5	17.433±0.014	0.39±1.4%
<i>g</i>	468.6	17.123±0.022	0.51±2.2%
<i>u</i>	355.1	17.358±0.022	0.43±2.2%
GALEX ^b – Ultraviolet			
NUV	227.1	17.07±0.03	0.54±3%
FUV	152.8	16.86±0.05	0.66±5%

^aK_s-band data are from CFHT WIRCam observations while J-band data are from Lick Gemini observations (see Section 2).

^bWIRCam and Gemini magnitudes are in the Johnson system. GALEX measurements are in AB magnitudes. GALEX uncertainties are as suggested in Morrissey *et al.* (2007).

Table 3. NIRC Fluxes For Background Galaxy Companion to Ton 345

Band	mag	Flux Density (μJy)
J	>21.0	<6.5
H	19.15 ± 0.24	$22.9 \pm 22\%$
K _s	18.47 ± 0.15	$27.3 \pm 14\%$

Note. — The background galaxy at $1.8''$ separation from Ton 345 appears to be a J-band drop-out galaxy. Comparing to galaxy models (e.g., see Figure 11 of Sanders *et al.* 2007, and references therein) suggests that this is a Balmer-break Spiral or Cool ULIRG galaxy at a redshift $z \sim 2$.

Table 4. HIRES Observations Summary

UT Date	Setup	Coverage	Integration Time (sec)	S/N ^a
SDSS1228				
05 May 2007	UV Collimator	3120-5950 Å	3000	22
14 Nov 2008	Red Collimator	4500-9000 Å	1800	12
15 Nov 2008	Red Collimator	4500-9000 Å	1600	13
16 Nov 2008	Red Collimator	4500-9000 Å	1900	12
Ton 345				
13 Feb 2008	UV Collimator	3130-5960 Å	2×1800	38 ^b
14 Feb 2008	UV Collimator	3130-5960 Å	2×1500	38 ^b
26 Feb 2008	Red Collimator	4600-9150 Å	3600	42
14 Nov 2008	Red Collimator	4500-9000 Å	2×1800	45 ^b
16 Nov 2008	Red Collimator	4500-9000 Å	1800	32
SDSS1043				
05 May 2007	UV Collimator	3120-5950 Å	3000	13
15 Nov 2008	Red Collimator	4500-9000 Å	2×2000	18 ^b
16 Nov 2008	Red Collimator	4500-9000 Å	1500 & 1700	14 ^b

Note. — A resolving power of $\sim 40,000$ was measured for all epochs from the FWHM of single arclines in comparison spectra.

^aS/N measured at 5750 Å.

^bS/N for combined exposures.

Table 5. Gas-disk Emission Line Measurements

Transition	UT Date ^a	Equivalent Width (Å)	Peak Separation ^b (km s ⁻¹)	Full Width ^c (km s ⁻¹)	Peak Midpoint Velocity ^b (km s ⁻¹)	$v_{\max}\sin i^b$ (km s ⁻¹)
SDSS 1228						
Ca II K	05 May 2007	0.6±0.1	707±20	1014±44	-35±10	455±23/559±38
Ca II H	05 May 2007	— ^f	731±18	1020±53	-22±9	489±38/531±38
Fe II $\lambda 5169$ ^g	05 May 2007	1.3±0.1	—	—	—	—
	14,15,16 Nov 2008	1.3±0.1	—	—	—	—
Ca II $\lambda 8498$	14,15,16 Nov 2008	13.8±1.0	656±9	938±16	-22±4	379±7/560±14
Ca II $\lambda 8542$	14,15,16 Nov 2008	19.3±1.4	655±9	944±9	-17±4	393±7/551±14
Ca II $\lambda 8662$	14,15,16 Nov 2008	19.8±1.7 ^e	659±5	933±35	-18±3	382±7/548±35
Ton 345						
Fe II $\lambda 5169$	13,14,26 Feb 2008 ^d	1.1±0.2	838±14	1349±87	-79±14	—
	14,16 Nov 2008	1.1±0.2	869±18	1305±96	-69±18	—
Ca II $\lambda 8498$	26 Feb 2008	5.2±0.4	842±20	1305±49	-90±11	671±35/634±35
	14,16 Nov 2008	4.9±0.4	827±18	1252±73	-104±8	619±18/634±71
Ca II $\lambda 8542$	26 Feb 2008	4.1±0.3	857±16	1281±63	-98±8	706±35/575±53
	14,16 Nov 2008	3.5±0.3	891±13	1211±56	-89±6	618±18/593±53
Ca II $\lambda 8662$	26 Feb 2008	3.4±0.2	876±17	1298±75	-99±9	663±28/635±69
	14,16 Nov 2008	3.4±0.5 ^e	882±25	1263±71	-89±12	611±17/652±69
SDSS1043						
Ca II $\lambda 8498$	15,16 Nov 2008	7.0±0.5	757±38	1482±50	39±19	786±35/686±35
Ca II $\lambda 8542$	15,16 Nov 2008	7.0±0.6	778±49	1439±50	52±25	811±35/628±35
Ca II $\lambda 8662$	15,16 Nov 2008	8.1±1.2 ^e	806±48	1402±109	42±24	802±104/600±35

^aSpectra have been combined when multiple days are listed.

^bSee Sections 3.2 and 5 for description of these quantities. The two different values reported for $v_{\max}\sin i$ correspond to the maximum velocity gas seen in the blue and red wings of the double-peaked emission features, respectively.

^cFull velocity width of emission feature, from continuum blueward of the blue emission peak to continuum redward of the red emission peak.

^dTo within the noise of each individual exposure the 13,14 Feb 2008 and 26 Feb 2008 Fe II $\lambda 5169$ emission features for Ton 345 are identical; to improve the S/N we combine all three spectra into a single 2008 Feb epoch.

^eMeasurement may be contaminated by second order blue light leak, see Section 2.4.

^fPhotospheric Balmer H ϵ absorption in SDSS1228 prevents an accurate continuum estimation for the Ca II H emission complex.

^gThe Fe II $\lambda 5169$ emission in SDSS1228 shows peculiar features (see Figure 4), the origin of which are uncertain. As such we do not include these measurements in this table.

Table 6. Kinematics of Gas-disk White Dwarfs

WD Name	$RV_{\text{obs}}^{\text{a}}$ (km s $^{-1}$)	M_{WD} (M_{\odot})	R_{WD} (R_{\odot})	$v_{\text{grav}}^{\text{b}}$ (km s $^{-1}$)	Distance (pc)	pmRA (mas yr $^{-1}$)	pmDE (mas yr $^{-1}$)	U (km s $^{-1}$)	V (km s $^{-1}$)	W (km s $^{-1}$)
SDSS1228	+37 \pm 4	0.77	0.011	+44	125 \pm 13	−44.0 \pm 2.0	−18.0 \pm 1.0	−18	−20	−12
Ton 345	+36 \pm 4	0.70	0.010	+44	85 \pm 10	−10.0 \pm 1.0	−62.0 \pm 2.0	+9	−21	−14
SDSS1043	+39 \pm 4	0.67	0.012	+35	185 \pm 19	+38.0 \pm 6.0	−46.0 \pm 4.0	+45	−27	+6

^a RV_{obs} is the observed radial velocity as measured from the absorption lines of each white dwarf. It has not been corrected for each white dwarf’s gravitational redshift.

^bGravitational redshift as computed from the model-determined mass and radius reported for each white dwarf in columns 3 and 4.

Note. — See Section 3.2 for discussion of input and output parameters. For the UVW space motions positive U is towards the Galactic center, positive V is in the direction of Galactic rotation, and positive W is toward the north Galactic pole.

Table 7. Dust Disk Models

	SDSS1228			Ton 345	SDSS1043
Stellar Parameters					
T _{eff} (K)	22,020			18,600	18,330
R _{WD} /Dist	2.0×10^{-12}			2.6×10^{-12}	1.5×10^{-12}
Disk Parameters ^a					
T _{inner} (K)	1100	1300±50	1350	1500	1200
T _{outer} (K)	700	500±70	350	1000	1100
<i>i</i> (°)	60	73±3	76	66	60

^aThe three different parameter sets for SDSS1228 correspond to the three curves plotted in Figure 6. The parameters are for the red, black, and blue curves respectively. We adopt the middle parameter set (having T_{inner} of 1300 K) for SDSS1228’s dust disk properties (corresponding to the black curve in Figure 6). From the three curves we estimate the 1σ uncertainties on the model parameters (see Section 4) which are reported with SDSS1228’s best fit parameters.

Note. — The effective temperatures for the three white dwarfs come from Gänsicke *et al.* (2006, 2007, 2008a). The ratio of the radius of the white dwarf to the distance of the white dwarf from Earth, $R_{\text{WD}}/\text{Dist}$; temperature at the inner edge of the disk, T_{inner} ; and inclination angle, i , come from the model fit to the UV, optical, and infrared photometry. See Section 4 for a discussion of the temperature at the outer edge of the disk (T_{outer}).

Table 8. Disk Dimensions

Name	v_{\max} (km s $^{-1}$)	Gas Disks		Dust Disks		
		$R_{inner,gas}$ (R _{WD})	$R_{outer,gas}$ (R _{WD})	$R_{inner,dust}$ (R _{WD})	$R_{outer,dust}$ (R _{WD})	T_{outer} (K)
SDSS1228	575 \pm 17	40 \pm 3	108	26 \pm 2	93 \pm 17	500
Ton 345	709 \pm 20	27 \pm 2	\sim 100	17 \pm 2	100 \pm 18	400
SDSS1043	923 \pm 52	12 \pm 2	81	23 \pm 2	80 \pm 15	470

Note. — All quoted uncertainties are 1σ (see below). *Gas disks*: v_{\max} comes from the average of the blue or red wing values (whichever is higher) listed in the “ $v_{\max}\sin i$ ” column of Table 5. This average value is then divided by the sine of the inclination angle reported in Table 7. $R_{inner,gas}$ is derived directly from the value reported in the “ v_{\max} ” column. The quoted uncertainties for $R_{inner,gas}$ also include the statistical uncertainties for the white dwarf masses and radii as quoted in Gänsicke *et al.* (2006, 2007, 2008a). There may be additional systematic uncertainties that are not included. $R_{outer,gas}$ is taken from Gänsicke *et al.* (2006, 2007, 2008a,b). *Dust disks*: See Section 4 for a description of how $R_{inner,dust}$ and $R_{outer,dust}$ are derived. T_{outer} corresponds to the outer dust radius shown. The uncertainties for $R_{inner,dust}$ and $R_{outer,dust}$ are estimated from the range of possible disk parameters modeled for the SDSS1228 data set and the suggested uncertainty for each star’s effective temperature as quoted in Gänsicke *et al.* (2006, 2007, 2008a).

Table 9. Ca II Emission Line Flux

Name	Ca II K	Ca II λ 8498	Ca II λ 8542	Ca II λ 8662	Ratio $F_{\text{IRT}}/F_{\text{HK}}$	Gas Disk Temperature (K)
	Total Line Flux ^a (10^{-15} ergs cm $^{-2}$ s $^{-1}$)					
SDSS1228	1.4	2.6	3.6	3.7	~ 3.5	~ 5000
Ton 345	$< 2.5^{\text{b}}$	1.8	1.3	1.2	$> 0.9^{\text{b}}$	< 6500
SDSS1043	$< 0.6^{\text{b}}$	0.7	0.7	0.8	$> 2.0^{\text{b}}$	< 6000

^aThese values are computed by multiplying emission line EW measurements reported in Table 5 by the stellar continuum flux at the emission line location.

^bThese upper limits are calculated assuming we could not detect Ca II H & K emission features weaker than those seen in SDSS1228 (see Figure 3).

Note. — See Section 6 for discussion.